

# Supporting Information:

## The true corrugation of a h-BN nanomesh layer

L. H. de Lima,<sup>1,2</sup> T. Greber,<sup>3</sup> and M. Muntwiler<sup>2</sup>

<sup>1</sup>*Centro de Ciências Naturais e Humanas, Universidade Federal do ABC, Santo André, 09210-580, Brazil*

<sup>2</sup>*Photon Science Division, Paul Scherrer Institut, 5232 Villigen PSI, Switzerland*

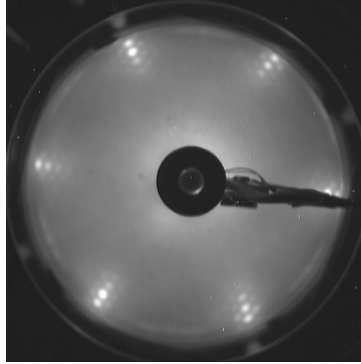
<sup>3</sup>*Physik-Institut, Universität Zürich, 8057 Zürich, Switzerland*

(Dated: 2020-01-25)

### EXPERIMENT

#### Sample Preparation

h-BN nanomesh on a Rh(111) single crystal is grown in ultra-high vacuum (base pressure  $2 \times 10^{-10}$  mbar) according to an established recipe [1–3]. First, the Rh(111) surface is cleaned by repeated cycles of Ar ion bombardment (1.0 keV) and annealing the crystal at 1150 K. The surface quality with respect to the presence of contaminants and ordering of the atoms is checked by x-ray photoelectron spectroscopy (XPS) and low-energy electron diffraction (LEED), respectively. Then, a monolayer of h-BN is grown by chemical vapour deposition (CVD), exposing the hot Rh surface (1050 K) to 80 Langmuir of borazine ( $\text{HBNH}_3$ ) ( $4.5 \times 10^{-7}$  mbar for 4 minutes). The quality of the h-BN preparation is confirmed by LEED, SI-Fig. 1. In our experience, the clarity of the superstructure spots in the LEED pattern is a very sensitive measure to check the growth quality and regularity of the nanomesh structure. The preparation of the sample has been repeated several times in preparation of the synchrotron beamtime until the quality known from previous LEED, XPS, ARPES, XRD and STM experiments has been reproduced. The photoelectron diffraction measurements were done once on the final sample.



SI-FIG. 1. Low-energy electron diffraction (LEED) pattern of the h-BN/Rh(111) sample showing the first-order and superstructure spots.  $E_{\text{kin}} = 60$  eV.

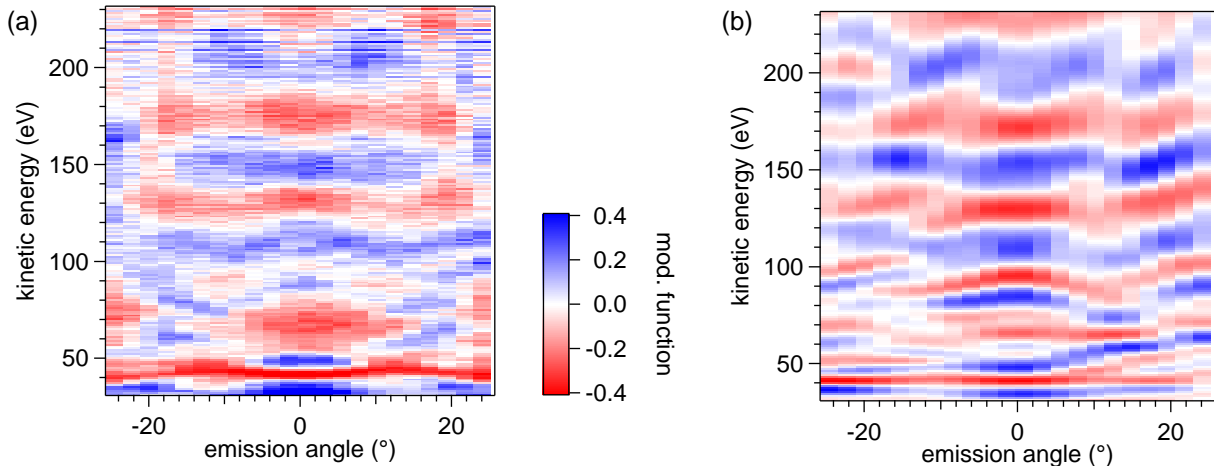
#### Data Acquisition and Reduction

The data acquisition and processing procedure for angle- and energy-scanned photoelectron diffraction at the PEARL beamline is described in detail in Ref. [4]. Briefly, photoelectrons are recorded by a Scienta EW4000 spectrometer with a two-dimensional detector as a function of kinetic energy  $E_{\text{kin}}$  and detection angle  $\alpha$ . The detection angle (orientation of entrance slit) is perpendicular to the scattering plane formed by the synchrotron beam and central axis of the analyser lens stack. The useful range of  $\alpha$  is  $40^\circ$  with an effective resolution of  $0.46^\circ$ .

For the XPD measurement (angle scan), the polar and azimuthal angles ( $\theta, \phi$ ) of the sample are varied with respect to the analyser lens axis, and  $I(E_{\text{kin}}, \alpha)$  spectra of the N 1s core level are collected at each angle. The  $\phi$  scan range is  $324^\circ$  in  $36^\circ$  steps, the  $\theta$  range  $84^\circ$  in  $2^\circ$  steps. The intensities  $I(\theta, \phi, \alpha)$  resulting from peak fitting are normalized and mapped to polar coordinates ( $\theta, \phi$ ) of the sample as described in Ref. [4]. The whole scan took 16.3 hours.

For the PhD measurement (energy scan),  $I(E_{\text{kin}}, \alpha)$  spectra of the N 1s core level are recorded for photon energies  $h\nu = 434 \dots 834$  eV in steps of 1 eV. The whole scan took 9 hours.

Modulation functions are obtained by normalization of the measured peak intensities as  $\chi = (I - N)/N$ , where the normalization function  $N$  is a smooth copy of the original data  $I$  calculated by a locally weighted regression (LOESS) [5]. The smoothing parameter is chosen large enough to preserve diffraction features but to remove slow variations due to photon flux, cross section and analyser transmission. For XPD, the normalization function is a function of  $\alpha$  and  $\theta$ , for PhD, a function of  $\alpha$  and  $h\nu$ .



SI-FIG. 2. Experimental and simulated PhD patterns of the pore component of the N 1s spectrum. (a) Experimental PhD pattern (modulation of intensity versus emission angle and kinetic energy). (b) Simulated PhD pattern for the best fitting atomic structure model. The R-factor of these data is 0.42.

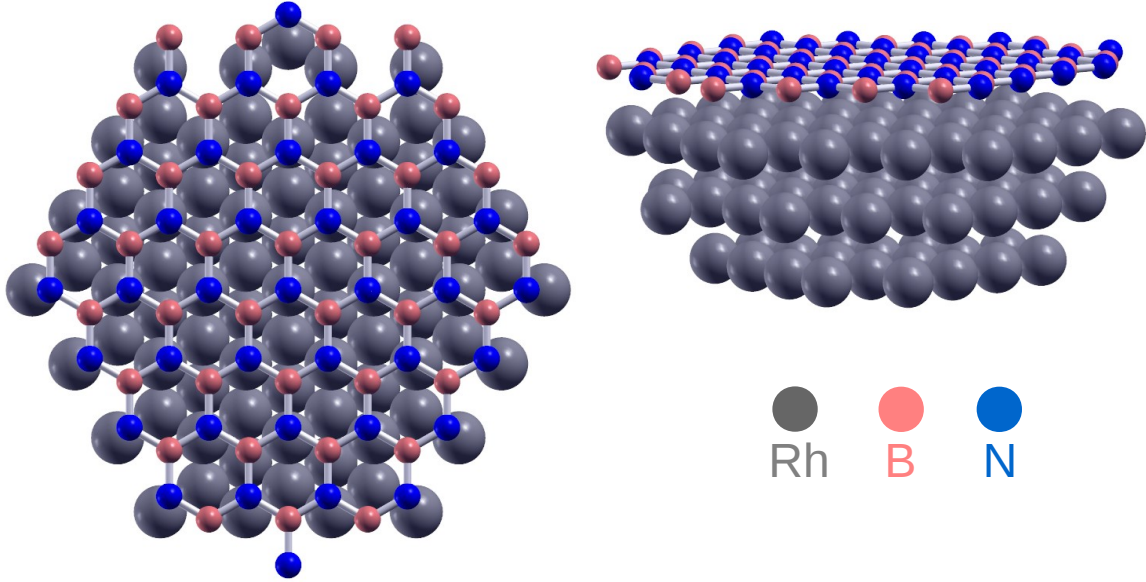
Note that we have acquired spectra as a function of detection angle  $\alpha$  for both XPD and PhD scans. While the wide acceptance angle of the detector is instrumental for reducing the acquisition time of XPD scans, the benefits for PhD are less obvious in the present case. Thus, for the R-factor optimization discussed in the main text, we have used only a  $2.5^\circ$  interval around normal emission. SI-Fig. 2 shows the full 2D modulation functions from experiment and simulation using the best model as optimized on the 1D modulation function. It can be seen that most experimental features are well reproduced by the simulation although some features appear sharper in the simulation. Due to these deviations the R-factor is 0.42 and considerably larger than for the 1D profile. We have found that the 1D profile is sufficient for the structural optimization and leads to a better convergence. This means that the 2D pattern in SI-Fig. 2 does not carry significantly more information than the beam at normal emission. This is expected because in the case of h-BN on a substrate, additional features appear at higher angles ( $\approx 30^\circ$ , see XPD pattern in Main-Fig. 2a) where backscattering from neighbouring atoms becomes more significant.

## MULTIPLE SCATTERING CALCULATIONS

### EDAC Calculations

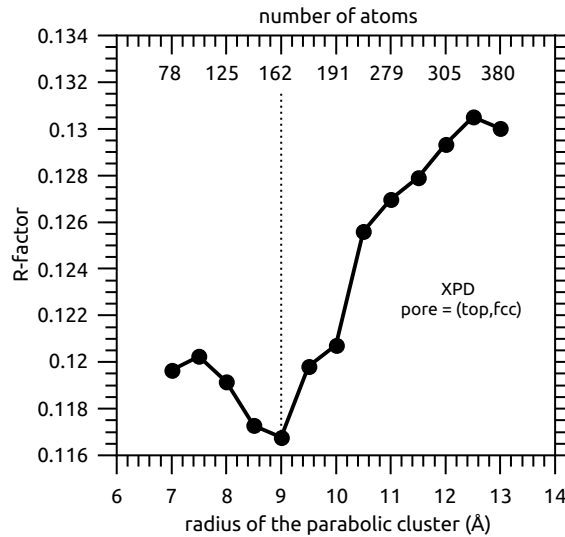
For a quantitative analysis, the XPD/PhD modulation patterns are compared to multiple scattering cluster calculations using the EDAC code [6]. As introduced in the main text (Fig. 2), we approximate our system with flat layers in one of three high-symmetry adsorption geometries with one emitter at the center. A justification for this approximation is given in a section further below. While, for clarity, Fig. 2 of the main text shows only the local geometry immediately surrounding the emitter atom, SI-Fig. 3 shows the actual cluster used for simulating the patterns of the pore peak in the (N,B) = (*top*,*fcc*) geometry.

The total number of atoms (1 h-BN and 3 Rh layers) depends on the in-plane radius of the parabolic cluster around the emitter atom. Initially, we treated the cluster radius as an additional variation parameter. We found that a radius of 3-4 lattice vectors, resulting in a  $18 \text{ \AA}$  wide cluster of about 160 atoms, gives the best match to the experiment. SI-Fig. 4 shows the R-factor as function of the cluster radius. A distinct minimum appears near  $9 \text{ \AA}$ .



SI-FIG. 3. Full cluster (162 atoms) used for calculating PED patterns of the  $(N,B) = (top, fcc)$  geometry in top view (left) and side view (right). The center atom is the only emitter. The in-plane lattice constants are fixed while the vertical positions of the N and B sublattices are variable.

The multiple-scattering expansion in EDAC is calculated with the recursion method up to a maximum of 25 iterations. We have verified that the final state wave function has converged at this recursion depth for a number of specific configurations. The scattering order is not limited in this approach and depends on two factors: First, the contribution of a particular scattering path is attenuated according to the universal curve of the inelastic mean free path [7]. Second, the *max. scattering path length* parameter (SI-Table I) filters scattering paths that contain segments longer than the given value. This parameter was kept variable during the optimizations. The maximum orbital angular momentum number used was  $l_{max} = 15$ . A finite acceptance angle of the photoelectron detector was included in the simulations, with a half-width angle of the acceptance cone of  $2^\circ$ . Finally, Debye-Waller attenuation was applied, where the Debye temperature was another optimization parameter. The experiments were done at room temperature.



SI-FIG. 4. R-factor as a function of the in-plane radius of the parabolic cluster, using the XPD/pore simulation.

### R-Factor Optimization

The structure is determined by variation of parameters and minimization of a reliability factor (R-factor) that is a measure of the agreement between theory and experiment. The R-factor is defined as

$$R = \min_{\alpha \in \mathbb{R}^+} \left[ \frac{\sum_i (\alpha \chi_{q,i} - \chi_{\text{exp},i})^2}{\sum_i (\alpha^2 \chi_{q,i}^2 + \chi_{\text{exp},i}^2)} \right] \quad (1)$$

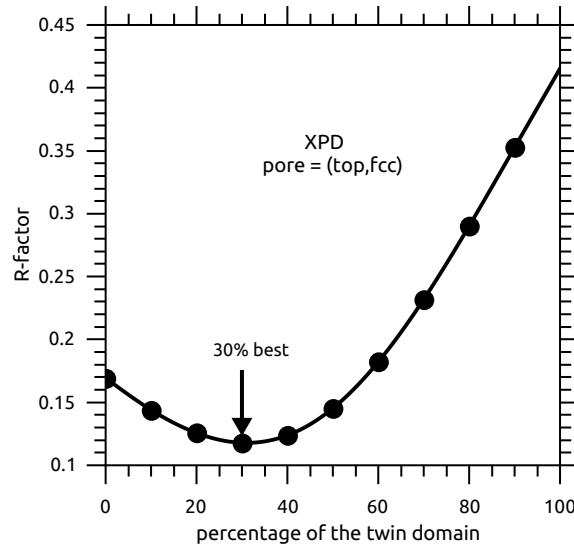
where  $\chi_{q,i}$  is the simulated modulation function for a tuple  $q$  of model parameters and data point  $i$  (angle or energy), and  $\chi_{\text{exp},i}$  is the corresponding experimental modulation function. The parameter  $\alpha$  is a single positive real number that is minimized separately in order to equalize the anisotropies of the experimental and simulated data sets.

The search algorithm is based on the efficient *particle swarm optimization* (PSO) for finding the global optimum in a multi-dimensional parameter space [8]. The algorithm is implemented in the PMSCO framework [9] that automates the optimization procedure on a high-performance cluster machine. The best structural and non-structural parameters obtained are summarized in SI-Table I.

SI-TABLE I. Optimal parameters determined with EDAC and PSO.

Parameter	pore $\Rightarrow$ (top,fcc)		wire $\Rightarrow$ (hcp,top)		wire $\Rightarrow$ (fcc,hcp)	
	XPD	PhD	XPD	PhD	XPD	PhD
interplanar distance N - Rh ( $\text{\AA}$ )	2.19	2.20	2.94	3.03	2.94	3.03
interplanar distance N - B ( $\text{\AA}$ )	0.07		0.01		0.01	
h-BN lattice constant ( $\text{\AA}$ )	2.502	2.504	2.501	2.507	2.505	2.509
Inner potential (eV)	24	22	25	21	18	21
Debye temperature (K)	496	397	248	164	181	152
Max scattering path length ( $\text{\AA}$ )	4.33	4.25	3.81	4.42	3.69	4.53
Position of the refractive surface ( $\text{\AA}$ )	0.95	0.91	0.95	0.93	0.94	0.93
Concentration of twin second domain	30%					

As mentioned in the main text, our sample contains a small amount of a twin domain rotated by  $180^\circ$ . The concentration of the minority domain can be determined in the same analysis of the XPD patterns, using the pore component, and amounts to 30%, as can be seen in SI-Fig. 5.

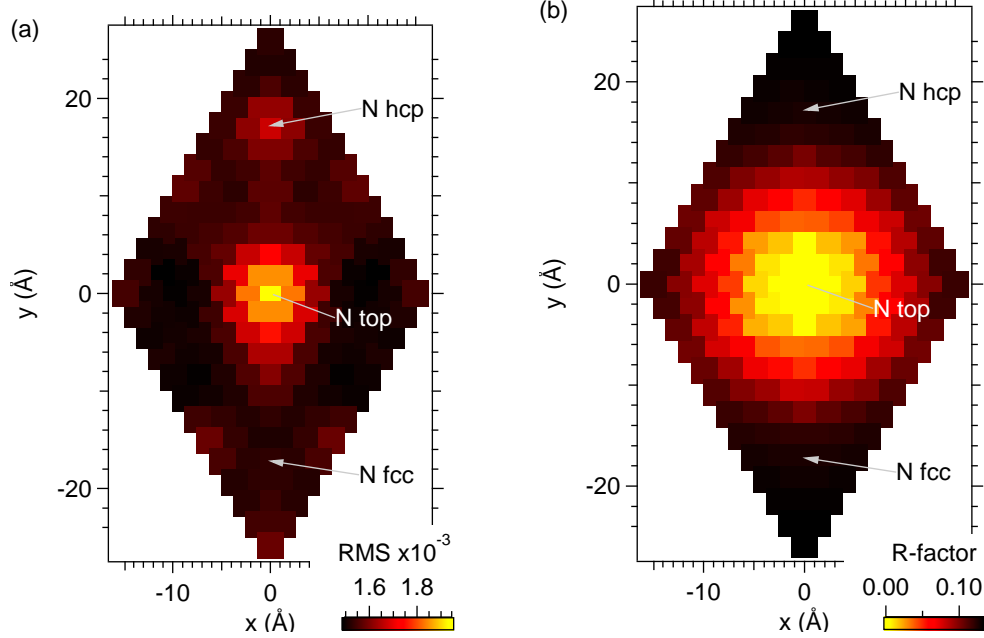


SI-FIG. 5. R-factor as a function of the twin second domain concentration, using the XPD/pore simulation.

### Diffraction signal from an incommensurate lattice

Considering only the lateral coordinates, the 13-on-12 superstructure leads to a variation of the local registry of the N and B atoms over the unit mesh, causing each of the 169 N emitters to be in a different local scattering geometry. Here we investigate which ones of the emitters contribute most to the measured signal. The result justifies the approximation made in the main text, where the measured signal is approximated with the contribution of a single emitter from the high-symmetry site of a flat h-BN layer.

SI-Fig. 6(a) shows the root-mean-square (RMS) values of the simulated PhD modulation function originating from each of the 169 N emitters at normal emission angle. (See Fig. 2(c) or 2(g) of the main text for an example of a modulation function.) It is evident that the (N,B) = (*top*,*fcc*) geometry, having the shortest distance between a N and a Rh atom, produces the strongest modulations whereas low-symmetry sites produce weaker modulations. The (*hcp*,*top*) and (*fcc*,*hcp*) geometries appear as local maxima.



SI-FIG. 6. Contributions of individual N emitters to the PhD modulation function. (a) RMS strength of the modulation function of each emitter in the supercell. The N top configuration is in the center of the graph, the other two high-symmetry sites are indicated. A high RMS value indicates a large contribution to the (spatially averaged) measured signal. (b) R-factor comparison of the emitter-average with the N top modulation function. The emitter average at each point includes all emitters lying at a smaller distance to the N top configuration.

For the average modulation function, not only the amplitude but also cancelling effects due to additional, differently registered emitters need to be considered. SI-Fig. 6(b) compares the modulation function of the N top emitter with an emitter average constructed by including all emitters that lie closer to the center of the pore. Within the pore region, the R-factor values vary from perfect agreement ( $R = 0$ ) at the center to about 0.05, which still indicates a close agreement. This means that the PhD signal of the pore peak is dominated by the contribution of the N top emitter at the center of the pore. The flat-layer approximation in our analysis is valid.

### ERROR ANALYSIS

The R-factor curves in Figure 2(d), 2(h) and 3 of the main text are obtained after the relaxation process, stepping only a selected structural parameter around their best value. The width of the curves is used to estimate the error of the respective parameter by fitting a quadratic function  $R(d) = R_{\min} + A(d - d_0)^2$ , where  $R_{\min}$  is the best R-factor,  $d$  the probed distance,  $d_0$  the best fit and  $A$  a coefficient that controls the curvature of the R-factor curve. Using this

function, the uncertainty is defined as

$$\delta d = \sqrt{\left(\frac{\delta R}{R_{\min}}\right) \frac{R_{\min}}{A}}. \quad (2)$$

Following Pendry's approach for LEED calculations [10], the term  $\delta R/R_{\min}$  can be determined by the number  $F$  of independent pieces of structural information contained in the measured data,  $\delta R/R_{\min} = \sqrt{2/F}$ . In our study, we estimate  $F \sim 80$  ( $\delta R/R_{\min} = 0.16$ ) for the XPD data set (angle scanned) and  $F \sim 15$  ( $\delta R/R_{\min} = 0.36$ ) for the PhD data set (energy scanned) by counting features in the data. The parameters resulting from this procedure are given in Table 2 of the main text.

- 
- [1] A. Nagashima, N. Tejima, Y. Gamou, T. Kawai, and C. Oshima, *Phys. Rev. B* **51**, 4606 (1995).
  - [2] M. Corso, W. Auwärter, M. Muntwiler, A. Tamai, T. Greber, and J. Osterwalder, *Science* **303**, 217 (2004).
  - [3] W. Auwärter, *Surf. Sci. Rep.* **74**, 1 (2019).
  - [4] M. Muntwiler, J. Zhang, R. Stania, F. Matsui, P. Oberta, U. Flechsig, L. Patthey, C. Quitmann, T. Glatzel, R. Widmer, E. Meyer, T. A. Jung, P. Aebi, R. Fasel, and T. Greber, *J. Synchrotron Rad.* **24**, 354 (2017).
  - [5] W. S. Cleveland, E. Grosse, and M.-J. Shyu, "Software for locally-weighted regression," <http://www.netlib.org/a/dloess> (1992).
  - [6] F. J. García de Abajo, M. A. Van Hove, and C. S. Fadley, *Phys. Rev. B* **63**, 075404 (2001).
  - [7] M. P. Seah and W. A. Dench, *Surf. Interface Anal.* **1**, 2 (1979).
  - [8] D. Duncan, J. Choi, and D. Woodruff, *Surf. Sci.* **606**, 278 (2012).
  - [9] M. Muntwiler, "PEARL multiple scattering cluster optimization for photoelectron diffraction experiments (PMSO)," <https://gitlab.psi.ch/pearl-public/pmsco> (2015).
  - [10] J. B. Pendry, *J. Phys. C: Solid State Phys.* **13**, 937 (1980).